

Sub-cycle multidimensional spectroscopy of strongly correlated materials

Received: 8 March 2023

Accepted: 12 December 2023

Published online: 24 January 2024

 Check for updatesV. N. Valmispild^{1,2}, E. Gorelov¹, M. Eckstein^{2,3,4}, A. I. Lichtenstein^{1,2,4},
H. Aoki^{5,6}, M. I. Katsnelson⁷, M. Yu. Ivanov^{8,9} & O. Smirnova¹⁰ ✉

Strongly correlated solids are complex and fascinating quantum systems, where new electronic states continue to emerge, especially when interaction with light triggers interplay between them. In this interplay, a sub-laser-cycle electronic response is particularly attractive as a tool for the ultrafast manipulation of matter at the petahertz scale. Here we introduce a new type of nonlinear multidimensional spectroscopy, which allows us to unravel charge and energy flows in strongly correlated systems interacting with few-cycle infrared pulses and the complex interplay between different correlated states evolving on the sub-femtosecond timescale. We demonstrate that the sub-cycle spectroscopy of a single-particle electronic response is extremely sensitive to correlated many-body dynamics and provides direct access to many-body response functions. For the two-dimensional Hubbard model under the influence of ultrashort, intense electric-field transients, we resolve the sub-femtosecond pathways of charge and energy flows between localized and delocalized many-body states and the creation of a highly correlated state surviving after the end of the laser pulse. Our findings open the way towards a regime of imaging and manipulating strongly correlated materials at optical rates, beyond the multicycle approach employed in Floquet engineering, with the sub-cycle response being a key tool for accessing many-body phenomena.

The advent of attosecond pulses^{1–3}, attosecond spectroscopy^{4–13} and lightwave electronics^{14–28}, which aim to resolve and control light-driven electron motion on sub-laser-cycle timescales^{29–32}, has challenged our perception of reactivity—a capacity of atoms, molecules or solids to undergo changes triggered by an external agent. In chemistry, it prompted a quest for charge-directed reactivity, a chemical change driven by attosecond electron dynamics^{33–39}. A similar concept should exist in solids, where strong electron–electron correlations^{40–42} can lead to a rich variety of phase transitions and the appearance of new states of matter^{43–45} due to electronic response to intense light⁴⁶, including possible light-induced superconductivity^{47–49} or light control of the

electronic band structure^{50,51}. An intriguing direction to control the electronic states in strongly correlated materials relies on time-periodic perturbations^{52–54}, giving rise to the powerful concept of the Floquet engineering of quantum materials⁵⁵, which typically focuses on laser-cycle-averaged modifications of material properties. Experimental observation of the cycle-by-cycle build-up of the Floquet bands⁵⁶ and of the sub-cycle band structure modifications⁵⁰ are opening access to the sub-cycle-resolved electronic structures of light-driven solids. The sub-laser-cycle timescale is particularly relevant in strongly correlated systems: a typical on-site electron–electron interaction $U \approx 1$ eV corresponds to the timescale of the correlated electronic response to an

¹European XFEL, Schenefeld, Germany. ²Institute of Theoretical Physics, University of Hamburg, Hamburg, Germany. ³Department of Physics, University of Erlangen-Nuremberg, Erlangen, Germany. ⁴The Hamburg Centre for Ultrafast Imaging, Hamburg, Germany. ⁵Department of Physics, The University of Tokyo, Tokyo, Japan. ⁶National Institute of Advanced Industrial Science and Technology (AIST), Tsukuba, Japan. ⁷Institute for Molecules and Materials, Radboud University, Nijmegen, The Netherlands. ⁸Max-Born-Institut, Berlin, Germany. ⁹Department of Physics, Imperial College London, London, UK. ¹⁰Technische Universität Berlin, Berlin, Germany. ✉e-mail: smirnova@mbi-berlin.de

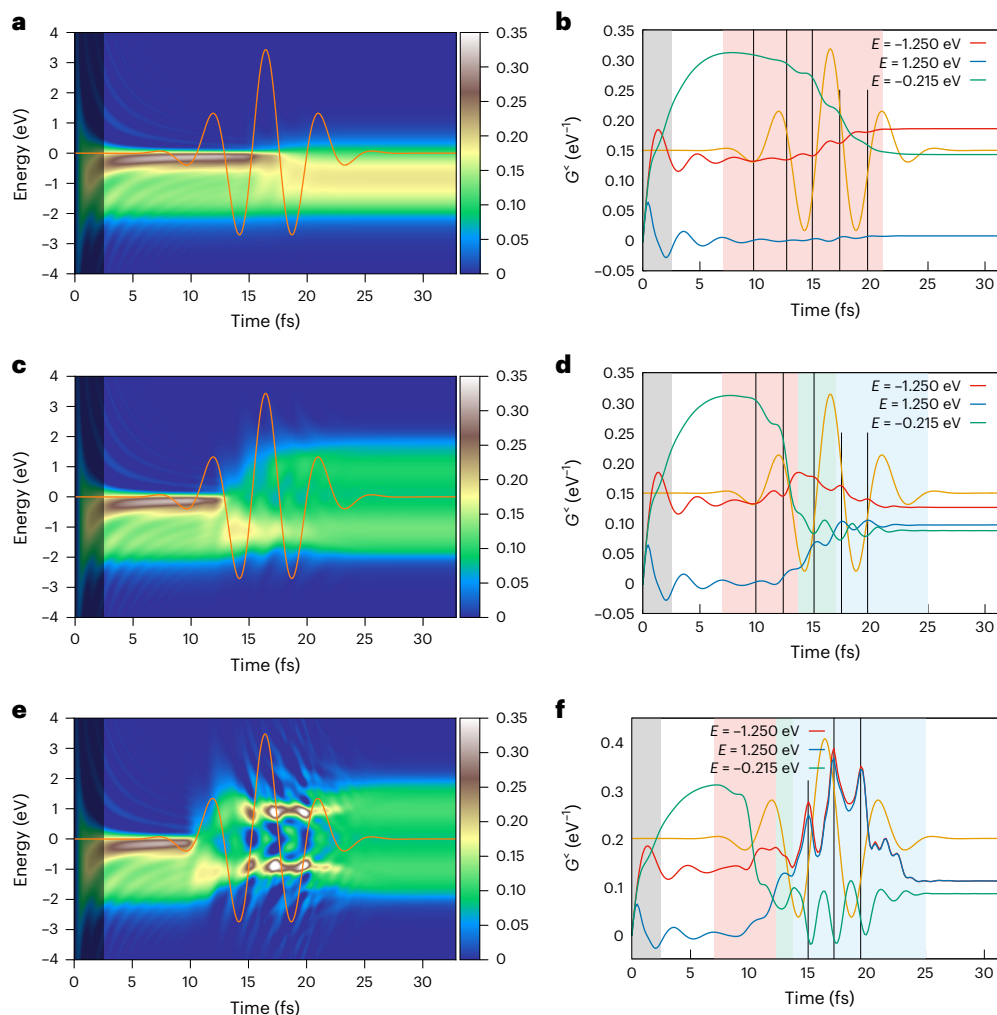


Fig. 1 | Temporal evolution of the density of states showing light-induced transition from metallic to Mott-insulating states. The orange curve shows the temporal profile of the laser pulse. **a, c, e**, $F_0 = 0.1 \text{ V A}^{-1}$ (**a**), $F_0 = 0.5 \text{ V A}^{-1}$ (**c**) and $F_0 = 2.0 \text{ V A}^{-1}$ (**e**). Artefact of the Fourier transform that appears in 0–2.5 fs is covered by a shadow. **b, d, f**, Oscillations of electron density at energies corresponding to the LHB ($E = -1.250 \text{ eV}$; red), UHB ($E = 1.250 \text{ eV}$; blue) and QP ($E = -0.215 \text{ eV}$; green)

for $F_0 = 0.1 \text{ V A}^{-1}$ (**b**), $F_0 = 0.5 \text{ V A}^{-1}$ (**d**) and $F_0 = 2.0 \text{ V A}^{-1}$ (**f**). The red, green and blue shadings mark three different regimes of field-driven dynamics. Red shading, density at LHB and UHB oscillates out of phase; blue shading, locking regime, density at LHB and UHB oscillates in phase; green shading, intermediate regime. The vertical lines indicate the maxima in LHB and UHB populations, correlated to the minima in QP populations in the locking regime.

external perturbation $\Delta t \approx 1/U \approx 1 \text{ fs}$, well below the cycle of a standard infrared (IR) driver, with the respective dynamics potentially leading to such remarkable features as a transition from Coulomb repulsion to effective electron–electron attraction induced by half-cycle pulses^{57,58}.

One way to probe and control the sub-cycle electronic response is to use few-cycle pulses with a controlled carrier–envelope phase (CEP)^{28–32,59}. In solids, these pulses have been used to detect photoemission delays⁶⁰; quantify the timescale of nonlinear response to light⁶¹; image surface states in topological insulators⁶²; and resolve and control highly nonlinear electronic response in bulk dielectrics, two-dimensional (2D) materials and nanostructures^{8,22,63–65}. Yet, the physical picture of electron–electron correlations evolving on the sub-cycle scale in strongly correlated systems remains elusive.

Here we introduce the sub-cycle multidimensional spectroscopy of electron dynamics in solids and apply it to a strongly correlated system. Our approach uses the CEP dependence of the correlated multi-electron response to decode the interplay between different many-body states, triggered by the interaction with a few-cycle mid-IR pulse. Ultimately, the analysis of the multidimensional spectra allows us to uncover the physical picture of the underlying correlated dynamics in this system, in both space and time. Fundamentally, we show that the sub-cycle spectroscopy of the one-particle response gives direct

access to many-body response functions. The possibility to analyse the underlying excitation pathways is key to understanding non-thermal materials control.

We consider a half-filled Hubbard model on the 2D square lattice for fermions, supporting a realistic 2D band dispersion with the characteristic Van Hove singularity and sharp band edges. The lattice is driven by a strong field linearly polarized along the lattice diagonal, triggering a fully 2D response (in contrast to previously employed Bethe or hypercube lattices^{66,67} or one-dimensional chains^{12,68}). To treat the non-perturbative time-dependent problem, we employ the non-equilibrium extension^{69–71} of the dynamical mean-field theory⁷². The method employed was benchmarked against the exact dynamical simulation of a one-dimensional finite chain¹², with excellent agreement, demonstrating the method’s ability to capture dynamical many-body correlations beyond the standard mean-field description (Supplementary Section 3). The algorithm is described in another work⁷³ (Methods). The implementation is based on the Non-Equilibrium Systems Simulation (NESSi) simulation package for non-equilibrium Green’s functions⁷⁴.

The parameters of the single-band Hubbard model are adjusted to reproduce the real electronic structure of undoped La_2CuO_4 : the lattice constant $a_0 = 3.78 \text{ \AA}$, the nearest-neighbour hopping $T_1 = 0.43 \text{ eV}$ (ref. 75)

and the Hubbard $U = 2.50$ eV (ref. 76). The specific value of $U/T_1 = 5.8$ in our case corresponds to the region of the largest many-body effects, according to the diagrammatic Monte Carlo analysis⁷⁷, and is close to U/T_1 for other cuprates^{78–80}. Our results, including the initial equilibrium state with a prominent maximum at the quasiparticle peak (QP) and featuring the lower Hubbard band (LHB) and upper Hubbard band (UHB) are, thus, characteristic for all the cuprate materials. We use few-cycle pulses centred at $\lambda = 1,500$ nm ($\omega = 0.827$ eV) and duration of 7.7 fs (full-width at half-maximum), with a total simulation time of 32.8 fs. To demonstrate that our results are typical for the low-frequency regime ($\omega < U$), we also present simulations for $\lambda = 3,000$ nm ($\omega = 0.413$ eV).

Figure 1a,c,e shows the temporal profile of the occupied density of states (Methods) for the field strengths F_0 from 0.1 to 2.0 V Å⁻¹ and $\omega = 0.827$ eV. Supplementary Section 5 shows the temporal profile for $\omega = 0.413$ eV, together with the vertical one-dimensional cuts showing the density of states before, during and after the pulse.

At $F_0 \approx 0.1$ V Å⁻¹ ($J_0 \approx 1.6 \times 10^{11}$ W cm⁻²), the voltage across a unit cell approaches the hopping rate, $a_0 F_0 \approx T_1$. Thus, $F_0 \approx 0.1$ V Å⁻¹ could modify the effective hopping rate within the laser cycle and alter the structure of the correlated system. Indeed, the transfer of spectral weight from the prominent maximum at the QP (located near the zero energy) before the onset of the laser pulse to the Hubbard bands during the laser pulse becomes prominent as soon as F_0 approaches 0.1 V Å⁻¹ (Fig. 1a). After the transition at -17.5 fs, the spectral density remains predominantly in the LHB and does not return to the QP after the pulse ends. Already for this field, Fig. 1a shows the importance of the sub-cycle response: the cycle-averaged renormalized hopping $T_1 \rightarrow T_1 J_0(F_0 a_0/\omega) = 0.97 T_1$ does not lead to any substantial changes in the spectral density, let alone to the major restructuring observed in Fig. 1a (Supplementary Sections 1 and 2). This result shows how the fast multielectron response ($U \gg \omega$) ‘teams up’ with the sub-cycle suppression of hopping T_1 to trigger the long-term restructuring of the correlated spectral density towards the state requiring $U/T_1 \geq 8$ in the field-free case.

At higher fields (Fig. 1c,e), we see a substantial transfer of the spectral density to the UHB (situated at $E = 1.25$ eV), with the electron density peaking at energies corresponding to the UHB and LHB. Crucially, this dichotomic structure survives well after the end of the pulse. Thus, Fig. 1a,c,e signifies the transition from a metallic to a highly correlated state in which the light-driven current is fully quenched (Fig. 4d).

To understand these complex many-body dynamics, we first look at the cuts (Fig. 1b,d,f) of the electron density for specific energies corresponding to the LHB ($E = -1.250$ eV), UHB ($E = 1.250$ eV) and QP (maximizing at $E = -0.215$ eV). The exchange of population (Fig. 1d) has three distinct regimes, marked as three shaded areas (Fig. 1b,d,f): around 4–11 fs (red), 11–16 fs (green) and beyond 16 fs (blue). The first regime (red shading) shows decreasing electron density at the energy corresponding to the QP peak and increasing density at energies corresponding to the LHB and UHB (Fig. 1b), with the populations at the LHB and UHB energies oscillating out of phase (Fig. 1b). In the second regime (Fig. 1d, green-shaded area), the density at UHB energy increases, whereas the density at LHB energy decreases. The third regime is the most interesting as it directly precedes the phase transition: we observe in-phase oscillations of the electron density at UHB and LHB energies (Fig. 1d, blue-shaded area). At higher intensities, the electron densities at UHB and LHB energies are not only synchronized with the field oscillations but are also locked to each other: both populations are equal and oscillate exactly in phase ($t > 14$ fs; Fig. 1f, blue-shaded area). The maxima of these locked populations are synchronized with the minima in the density located at the QP and are correlated with the instantaneous laser-field oscillations. The locking of populations at the three key energies of the system is correlated with the onset of metal–insulator transition (Fig. 1c,e) and allows us to decode the pathways of charge and energy flows between the correlated states, as described below.

The cartoon in Fig. 2a illustrates the three key field-free many-body states of our system using the dynamical mean-field theory language⁸¹.

The characteristic many-body states contributing to the signal at the LHB mainly involve electrons localized on singly occupied lattice sites, QP represents the superposition of delocalized and localized electrons, and doubly occupied and unoccupied sites are the characteristic of many-body states contributing to the UHB. The analysis (Supplementary Section 2) shown in Fig. 1f suggests that the density oscillations at QP are in phase with the laser field: the minima coincide with $F(t) \approx 0$, and the maxima coincide with $|F(t)| \approx F_0$. The rate of flow of electron density from the LHB and UHB maximizes near zeros of field oscillation, whereas the rate of flow of electron density to the LHB and UHB maximizes near the instantaneous maxima of the field.

To decode the physics underlying these sub-cycle electron dynamics, we need a spectroscopy technique sensitive to such dynamics. To this end, we exploit the full spectroscopic nature of the one-particle Keldysh Green’s function $G^<(t, t - \tau)$, which describes two photoionization events delayed by τ . Formally, $G^<(t, t - \tau)$ in the presence of the IR field corresponds to a sequence of three pulses (Fig. 2b) reminiscent of—but not identical to—the setup of nonlinear 2D spectroscopy⁸². In this sequence, the intense low-frequency field plays the role of a control pulse, which modifies our system between the photoionization events at t and $t - \tau$. $G^<(t, \Omega_\tau)$ (Fig. 1) is the energy-domain counterpart of $G^<(t, t - \tau)$ (the Fourier transform of $G^<(t, t - \tau)$ with respect to τ). It can be retrieved from multipulse time- and angle-resolved photoemission experiments⁸³ (Supplementary Fig. 5) for the mapping between $G^<(t, \Omega_\tau)$ and the photoelectron spectra. Supplementary Section 4 provides a representative time-resolved photoelectron spectrum for the IR field with $\lambda = 3$ μ m, with sub-cycle dynamics resolved even by a 2.5 fs ionizing pulse owing to the long period of the IR driver. If we select a value of Ω_τ in $G^<(t, \Omega_\tau)$ and Fourier transform $G^<(t, \Omega_\tau)$ with respect to the delay t between the control pulse and pump–probe pair, we obtain the spectrum of the states (transition frequencies) that the Floquet state associated with Ω_τ couples to (Methods). Indeed, for the dynamics described by a single Floquet state, $G^<(t, \Omega_\tau)$ should periodically behave as a function of t , and its Fourier transform will only show the sidebands at $\pm n\omega$ (n is an integer; Fig. 2c, ladder of red–brown peaks). In contrast, in the presence of non-adiabatic transitions between the Floquet states, $G^<(t, \Omega_\tau)$ becomes aperiodic and its Fourier transform will show the new frequencies appearing due to non-adiabatic excitations (Fig. 2c, green peaks).

Next, we can reveal the underlying sub-cycle dynamics by scanning the CEP ϕ_{CEP} of the IR (control) pulse and recording the resulting response $G^<(t, t - \tau, t_{\text{CEP}})$ as a function of $t_{\text{CEP}} = \phi_{\text{CEP}}/\omega$. The Fourier transform of $G^<(t, t - \tau, t_{\text{CEP}})$ with respect to t_{CEP} shows the speed of response⁸⁴: from instantaneous to cycle averaged. The broader the resulting spectrum is with respect to the CEP (Fig. 2c shows the schematic), the stronger is the non-trivial CEP dependence and the stronger, faster and more sensitive to the instantaneous electric field are the non-adiabatic transitions between the Floquet states.

We now focus on non-adiabatic dynamics to highlight the part of the interaction that is fundamentally different from the cycle-averaged response. To this end, we consider the difference between the derivatives of Green’s function with respect to t and t_{CEP} , that is, $\Delta G_{ij}^<(t, t - \tau, t_{\text{CEP}})$ ($\Delta \equiv \frac{\partial}{\partial t} - \frac{\partial}{\partial t_{\text{CEP}}}$). Here $\Delta G_{ij}^<(t, t - \tau, t_{\text{CEP}})$ contains only non-adiabatic transitions and provides direct access to non-equilibrium two-particle dynamics via the respective Green’s functions $K_{ij\sigma}^{pm}(t, t - \tau)$ and $\tilde{K}_{ij\sigma}^{pm}(t, t - \tau)$ (Methods):

$$\begin{aligned} \Delta G_{ij\sigma}^< &= - \sum_{m,p} f(t - \tau) a_{mp}(t - \tau) K_{ij\sigma}^{pm}(t, t - \tau) \\ &- \sum_{m,p} f(t) a_{mp}(t) \tilde{K}_{ij\sigma}^{pm}(t, t - \tau) + \Delta G_{ij\sigma}^{(1)<}, \end{aligned} \quad (1)$$

where $f(t)$ is the envelope of the short pulse, $a_{mp}(t) = \langle \Psi_m(t) | \frac{\partial}{\partial t} | \Psi_p(t) \rangle$ is the amplitude of the non-adiabatic transition between the time-dependent states evolving from the field-free eigenstates $|\Psi_m(t_0)\rangle$

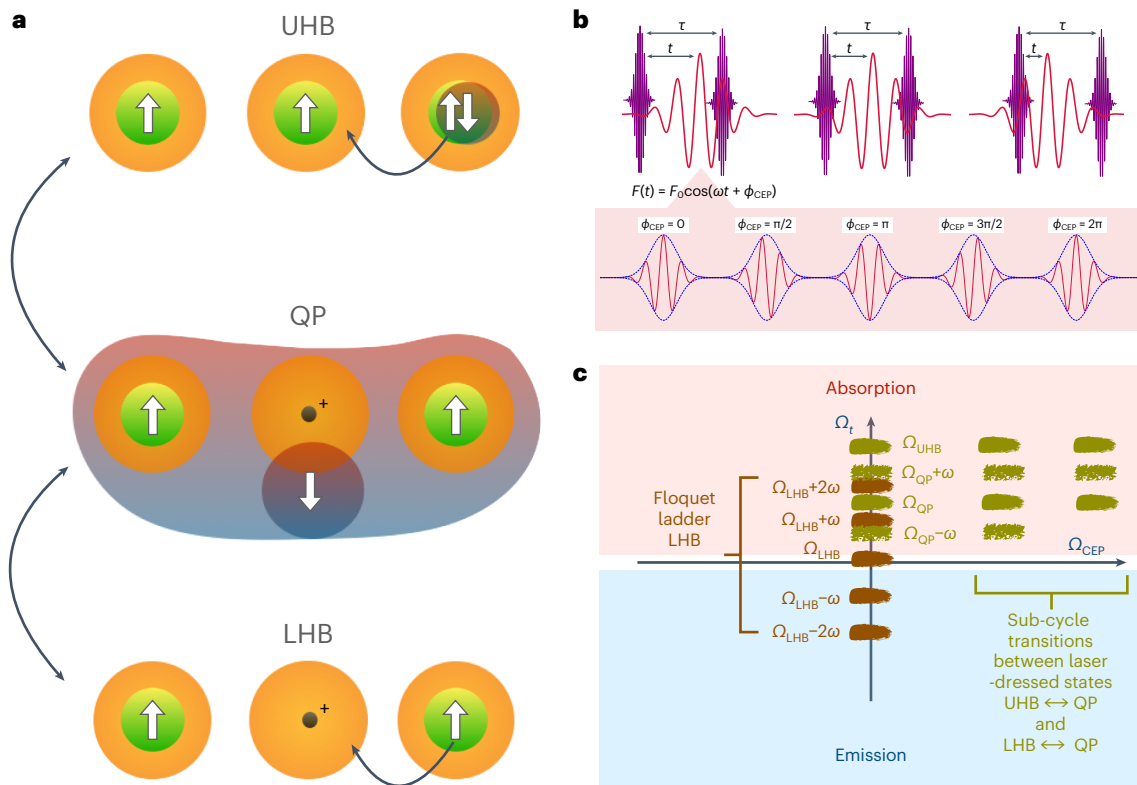


Fig. 2 | Spectroscopic nature of Keldysh Green's function G^c . **a**, Cartoon view of the key many-body states corresponding to the spectroscopic signal at energies of the LHB, QP and UHB. The orange circles stand for lattice sites; green circle, an electron localized on a lattice site; white arrows, orientation of electron spin; grey circle and grey cloud, a delocalized electron; and two oppositely oriented white arrows, a doubly occupied site. The double-headed arrows indicate the possible sub-cycle transitions driven by the field in the phase-locking regime (Fig. 1f). **b**, Scanning delay τ between the pump and probe pulses (violet) and delay t between the pump-probe pair and the control pulse (red) form a two-dimensional dataset for Green's function $G^c(t, t - \tau)$, emulating

the photoionization signal. Scanning the CEP (ϕ_{CEP}) of the control pulse yields the third dimension of the spectroscopic signal $G^c(t, t - \tau, t_{\text{CEP}})$. **c**, Fourier transform of $G^c(t, t - \tau, t_{\text{CEP}})$ with respect to all the arguments yields $G^c(\Omega_\tau, \Omega_t, \Omega_{\text{CEP}})$. A cartoon view of $|G^c(\Omega_\tau, \Omega_t, \Omega_{\text{CEP}})|$ for Ω_τ fixed at the energy corresponding to the LHB. The red-brown peaks illustrate the associated Floquet ladder representing the laser-dressed LHB state. The appearance of green peaks at $\text{QP} \pm n\omega$ and UHB is due to non-adiabatic transitions between the laser-dressed states, namely, $\text{LHB} \leftrightarrow \text{QP}$ and $\text{UHB} \leftrightarrow \text{QP}$. The extension of green peaks in the Ω_{CEP} dimension quantifies the sub-cycle response time.

and $|\Psi_p(t_0)\rangle$, $\Delta G_{ij}^{(1)<}$ are the non-adiabatic terms of one-particle nature and

$$K_{ij\sigma}^{pm}(t, t - \tau) = U \langle \Psi_p(t_0) | c_{i\sigma}^\dagger(t - \tau) n_{i\bar{\sigma}}(t - \tau) c_{j\sigma}(t) | \Psi_m(t_0) \rangle, \quad (2)$$

$$\tilde{K}_{ij\sigma}^{pm}(t, t - \tau) = U \langle \Psi_p(t_0) | c_{j\sigma}(t) n_{j\bar{\sigma}}(t) c_{i\sigma}^\dagger(t - \tau) | \Psi_m(t_0) \rangle. \quad (3)$$

Here U is the on-site Coulomb interaction, $c_{i\sigma}^\dagger$ ($c_{j\sigma}$) are the fermionic creation (annihilation) operators for site i (j) and spin σ , and $n_{i\sigma} = c_{i\sigma}^\dagger c_{i\sigma}$ is the particle number operator.

To visualize the non-adiabatic transitions encoded in $\Delta G^c(\Omega_\tau, \Omega_t, \Omega_{\text{CEP}})$, we fix Ω_τ and plot the resulting 2D spectrum $|\Delta G^c(\Omega_\tau, \Omega_t, \Omega_{\text{CEP}})|$ as a function of Ω_t (vertical axis) and Ω_{CEP} (horizontal axis) (Fig. 2c shows the schematic). Figure 3 shows the respective 2D spectra $\Delta G^c(\Omega_\tau, \Omega_t, \Omega_{\text{CEP}})$ for three intensities and for $\Omega_\tau = -1.25$ eV (LHB) and $\Omega_\tau = 1.25$ eV (UHB). At the lowest field of $F_0 = 0.1 \text{ V \AA}^{-1}$ and for $\Omega_\tau = -1.25$ eV, the two peaks dominating the spectrum (Fig. 2a) at $\Omega_{\text{CEP}} = 0$ correspond to the LHB ($\Omega_t = 0$) and QP ($\Omega_t \approx 1.25$ eV). Figure 3b shows the 2D spectra for $\Omega_\tau = 1.25$ eV corresponding to the UHB, for the same F_0 . The dominant peak at $\Omega_{\text{CEP}} = 0$ corresponds to the contribution of QP, signifying transitions between QP and UHB.

At the intermediate field of $F_0 = 0.5 \text{ V \AA}^{-1}$ (Fig. 3c,d), the peaks at $\Omega_{\text{CEP}} = 0$ (Fig. 3c) (for $\Omega_\tau = -1.25$ eV; LHB) correspond to the Floquet ladders associated with both QP and LHB, with broad overlapping steps.

The CEP-sensitive dynamics becomes more important in the LHB-QP transitions. The dominant part of the upper peak at $\Omega_{\text{CEP}} = 2\omega$ is due to the QP lifted by one photon or UHB.

In the spectroscopic portrait of the system in the high-field regime ($F_0 = 2 \text{ V \AA}^{-1}$), Fig. 3e,f contains several new features. First, we see a broad spectrum along the vertical axis (Ω_t) for a wide range of the horizontal axis (Ω_{CEP}). Second, the sub-cycle dynamics is very important and the spectrum has individual sub-cycle cut-offs: the highest positive and highest negative Ω_t depend on Ω_{CEP} . These cut-offs appear to be proportional to the instantaneous values of the laser field and increase with increasing $\Omega_{\text{CEP}} > 0$. Third, the overall 2D spectra are shifted towards positive values of Ω_t for LHB (corresponding to absorption) and negative values of Ω_t for UHB (corresponding to emission). The respective peaks at $\Omega_{\text{CEP}} = 4\omega$ (Fig. 3e) and $\Omega_{\text{CEP}} = -4\omega$ (Fig. 3f) indicate their strongly sub-cycle nature. Fourth, although the direct non-adiabatic transitions between LHB and UHB (Fig. 3e, orange circles) become visible, the non-adiabatic transitions are still dominated by the $\text{LHB} \leftrightarrow \text{QP}$ and $\text{UHB} \leftrightarrow \text{QP}$ couplings.

Indeed, the onset of locking is synchronized with the saturation of energy transfer from the field to the system (Fig. 4a). For the highest field ($F_0 = 2 \text{ V \AA}^{-1}$), the maximum energy saturates at zero. The onset of locking (Fig. 4c) is accompanied by the suppression of current (Fig. 4d), which is fully quenched at -18 fs (Fig. 4c,e) when the insulating state is established. Note that Fig. 4c,d shows the lower laser frequency of $\omega = 0.413$ eV, demonstrating that our results are independent of the frequency of the non-resonant field.

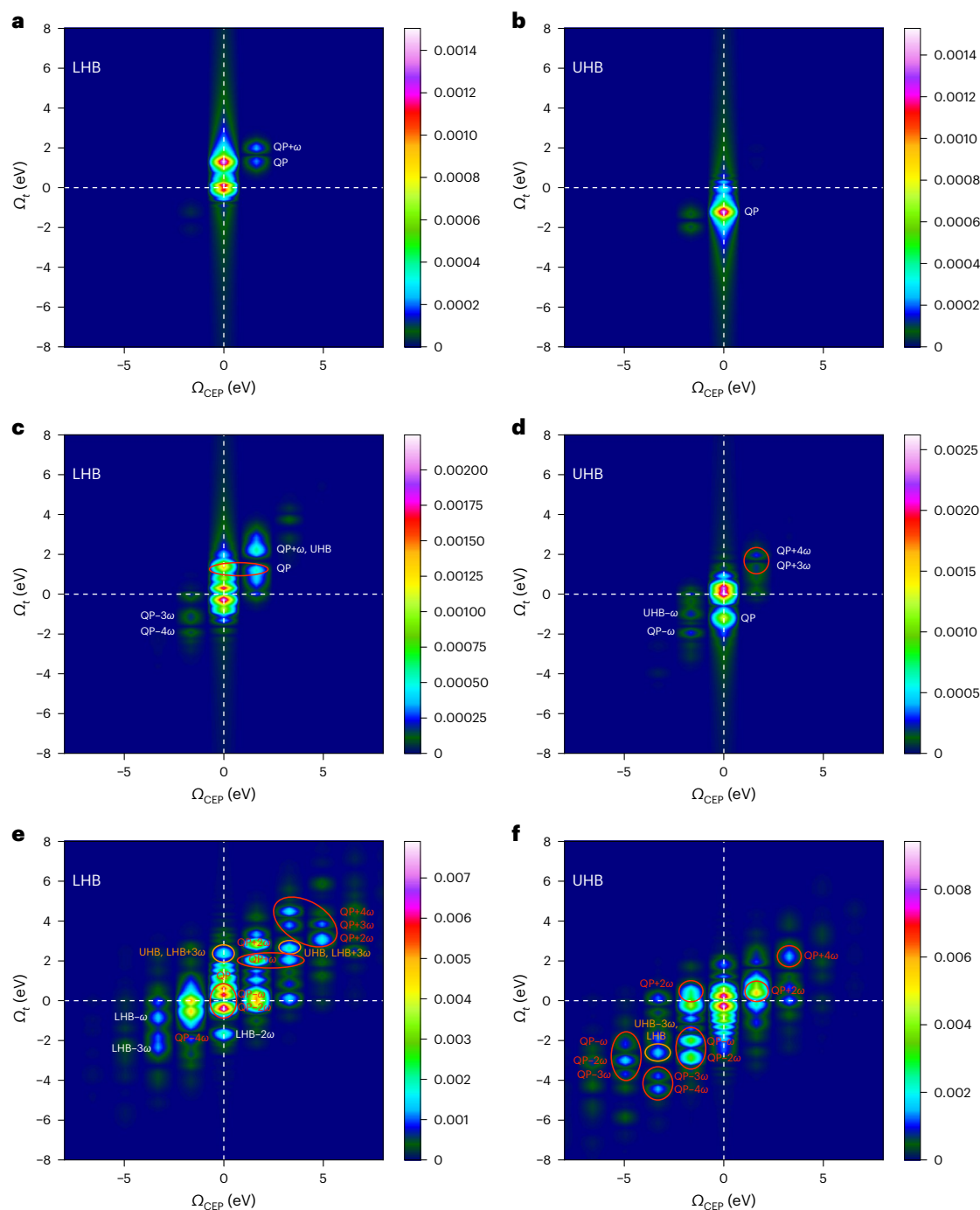


Fig. 3 | Multidimensional spectroscopy of correlated electron dynamics. a–f, $|\Delta G^{(3)}(\Omega_r, \Omega_r, \Omega_{\text{CEP}})|$ versus $\Omega_r, \Omega_{\text{CEP}}$ for $\Omega_r = -1.25$ eV (LHB) (a, c and e) and $\Omega_r = 1.25$ eV (UHB) (b, d and f) and for different field strengths of $F_0 = 0.1$ V Å⁻¹ (a and b), $F_0 = 0.5$ V Å⁻¹ (c and d) and $F_0 = 2$ V Å⁻¹ (e and f).

This spectroscopic information points to the following simplified picture of many-body dynamics in the locking regime. The synchronized cycling of charge flow along the two ‘circuits’, namely, LHB → QP → LHB and UHB → QP → UHB, appears to dominate the dynamical photon-dressed many-body state just before it freezes into the final state after the end of the laser pulse. At the peak of the field, a localized electron in the LHB is promoted to the QP, leaving an empty site behind. At the same time, the strong field also destroys doublons: a doublon from the UHB loses one of its electrons into the QP. The total energy does not change during these two synchronized processes. Near the instantaneous zero of the field, the QP electrons localize on the empty or half-filled sites of the lattice completing the oscillation

cycle: localization at an empty site contributes to the population in the LHB, whereas localization at a half-filled site contributes to the population in the UHB. However, in contrast to light-driven dynamics in dielectrics¹¹, the flow of charge between LHB and QP or UHB and QP cannot be understood as a single-electron oscillation.

Indeed, the time evolution of double occupancy (Fig. 4b) shows that in the locking regime, the doublon production saturates at 0.25—the maximum value for an uncorrelated system. Thus, every produced doublon decays and its fragments randomly occupy lattice sites. This ‘randomness’ limits the total energy increase to zero energy and precludes population inversion, that is, achieving a higher electron density at the UHB compared with LHB. This apparent randomness could be

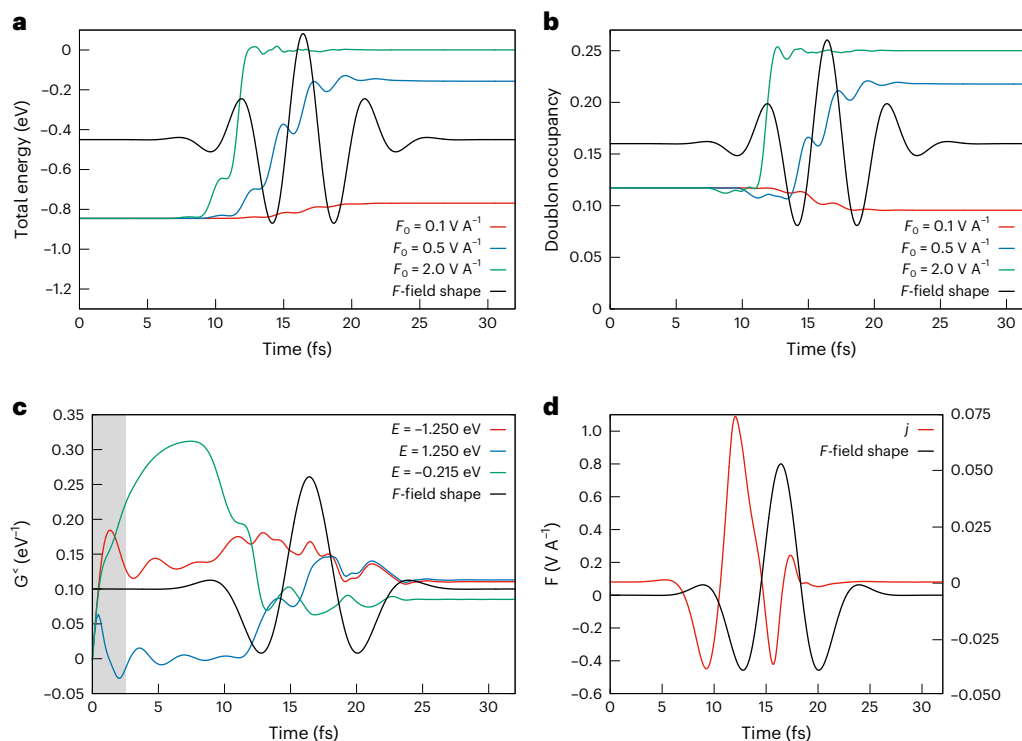


Fig. 4 | Temporal dynamics of metal–insulator transition. **a,b**, Time-resolved total energy (**a**) and doublon occupancy (**b**) for $\omega = 0.827$ eV and various field strengths, namely, $F_0 = 0.1$ V A $^{-1}$ (red), 0.5 V A $^{-1}$ (blue) and 2.0 V A $^{-1}$ (green). **c,d**, Metal–insulator transition driven by the laser field carried at $\omega = 0.413$ eV.

Oscillations of electron density at energies corresponding to the LHB ($E = -1.250$ eV; red), UHB ($E = 1.250$ eV; blue) and QP ($E = -0.215$ eV; green) for $F_0 = 0.8$ V A $^{-1}$ (**c**). Laser pulse (black) and current (red) (**d**). The onset of locking regime at 18 fs (**c**) coincides with the quenching of current (**d**).

a sign of entanglement destroyed by our observation. For example, calculating the double occupancy, we trace out a multitude of different ways in which doublons are created and destroyed in each laser cycle, that is, we do not follow their individual Feynman paths when calculating this observable, and therefore, we partially destroy the entanglement in our system.

In correlated systems, a large increase in the electron temperature can transform a metal into a bad metallic or insulating-like state. However, in our case, the opening of the gap and the peculiar dynamics already observed within a small fraction of the laser cycle is clearly not thermal. In contrast to phonon-driven transitions⁸⁵, our mechanism is purely electronic.

Our results show the power of the sub-cycle response to record and address non-equilibrium many-body dynamics. Here we considered the first derivative with respect to $\Delta \equiv \frac{\partial}{\partial t} - \frac{\partial}{\partial t_{\text{CEP}}}$, which gave us access to non-equilibrium two-particle correlations. Likewise, the n th derivative, Δ^n , contains the non-equilibrium n -particle Green's functions. If the correlations are strong, as is the case here, odd and even multiphoton pathways contributing to the CEP-dependent response can involve photon absorption by different electrons, with correlated interaction establishing coherence between these interfering events. Note that in contrast to the standard equilibrium (diagonal in m) expression for the two-particle Green's functions, namely, $K_{ij\sigma}^{mm}(t, t - \tau)$ and $K_{ij\sigma}^{mm}(t, t - \tau)$, $\Delta G_{ij}^{<}$ features non-equilibrium two-particle correlations, which would not be recorded in long pulses, as $\Delta G_{ij}^{<} = 0$ in this case, corresponding to the standard Floquet regime.

Our current setup corresponds to attosecond pulses performing photoionization and a strong IR pulse controlling the phase transition. The carrier of the IR pulse is well below the work function and the required IR-field strengths are also below the range where the field induces material breakdown. To probe the shells of interest, we envision a pair of sub-femtosecond vacuum ultraviolet–extreme ultraviolet pulses in the range of 20–30 eV; such pulse pairs have now become

available⁸⁶. The experiment can also be performed with attosecond pulse trains leading to the RABBIT⁸⁷ method, which also gives access to the phase of the photoionization spectrum and thus to Green's functions analysed in this Article. The experiments envisioned here are now becoming realistic, owing to remarkable advances in the generation of high-energy sub-femtosecond waveforms^{86,88} and attosecond interferometry including the generation of two phase-locked attosecond pulses with attosecond timing with respect to each other⁸⁹, full control of polarization (parallel or perpendicular), attosecond lock with respect to the generating IR pulse^{90,91} and temporal resolution well below 1 fs. Another example is the waveform synthesis technology developed in attosecond picoscopy⁶⁵.

Our findings demonstrate the possibility of manipulating the phases of correlated systems with strong non-resonant fields on the sub-cycle timescale, in a manner that is robust against the frequency of the driving field. Even though such non-resonant light-induced modifications of the electronic structure vanish in atoms or molecules once the light is turned off, in a strongly correlated system, light-induced reshaping of the electron density can lead to persistent modifications surviving after the end of the pulse, as we see here. The pulse can, thus, transfer the system into a correlated state inaccessible under equilibrium conditions between electrons and lattice, with non-adiabatic transitions triggering non-equilibrium many-body correlations (equation (2)). The achieved final state is controlled by charge density and currents shaped on the sub-laser-cycle timescale; the spectroscopy introduced here can provide key insights in analysing and designing such excitation pathways.

Online content

Any methods, additional references, Nature Portfolio reporting summaries, source data, extended data, supplementary information, acknowledgements, peer review information; details of author contributions and competing interests; and statements of data and code availability are available at <https://doi.org/10.1038/s41566-023-01371-1>.

References

- Kienberger, R. et al. Atomic transient recorder. *Nature* **427**, 817–821 (2004).
- Sansone, G. et al. Isolated single-cycle attosecond pulses. *Science* **314**, 443–446 (2006).
- Ferrari, F. et al. High-energy isolated attosecond pulses generated by above-saturation few-cycle fields. *Nat. Photon.* **4**, 875–879 (2010).
- Itatani, J. et al. Attosecond streak camera. *Phys. Rev. Lett.* **88**, 173903 (2002).
- Cavalleri, A. L. et al. Attosecond spectroscopy in condensed matter. *Nature* **449**, 1029–1032 (2007).
- Calegari, F. et al. Ultrafast electron dynamics in phenylalanine initiated by attosecond pulses. *Science* **346**, 336–339 (2014).
- Nisoli, M., Declève, P., Calegari, F., Palacios, A. & Martin, F. Attosecond electron dynamics in molecules. *Chem. Rev.* **117**, 10760–10825 (2017).
- Seiffert, L. et al. Attosecond chronoscopy of electron scattering in dielectric nanoparticles. *Nat. Phys.* **13**, 766–770 (2017).
- Pazourek, R., Nagele, S. & Burgdörfer, J. Attosecond chronoscopy of photoemission. *Rev. Mod. Phys.* **87**, 765 (2015).
- Dahlström, J., L’Huillier, A. & Maquet, A. Introduction to attosecond delays in photoionization. *J. Phys. B: At. Mol. Opt. Phys.* **45**, 183001 (2012).
- Vampa, G. et al. Linking high harmonics from gases and solids. *Nature* **522**, 462–464 (2015).
- Silva, R., Blinov, I. V., Rubtsov, A. N., Smirnova, O. & Ivanov, M. High-harmonic spectroscopy of ultrafast many-body dynamics in strongly correlated systems. *Nat. Photon.* **12**, 266–270 (2018).
- Silva, R., Jiménez-Galán, Á., Amorim, B., Smirnova, O. & Ivanov, M. Topological strong-field physics on sub-laser-cycle timescale. *Nat. Photon.* **13**, 849–854 (2019).
- Goulielmakis, E. et al. Attosecond control and measurement: lightwave electronics. *Science* **317**, 769–775 (2007).
- Jiménez-Galán, Á., Silva, R., Smirnova, O. & Ivanov, M. Lightwave control of topological properties in 2D materials for sub-cycle and non-resonant valley manipulation. *Nat. Photon.* **14**, 728–732 (2020).
- Jiménez-Galán, Á., Silva, R. E., Smirnova, O. & Ivanov, M. Sub-cycle valleytronics: control of valley polarization using few-cycle linearly polarized pulses. *Optica* **8**, 277–280 (2021).
- Borsch, M., Meierhofer, M., Huber, R. & Kira, M. Lightwave electronics in condensed matter. *Nat. Rev. Mater.* **8**, 668–687 (2023).
- Schiffrin, A. et al. Optical-field-induced current in dielectrics. *Nature* **493**, 70–74 (2013).
- Lange, C. et al. Sub-cycle control of terahertz high-harmonic generation by dynamical Bloch oscillations. *Nat. Photon.* **8**, 119–123 (2014).
- Rybka, T. et al. Sub-cycle optical phase control of nanotunnelling in the single-electron regime. *Nat. Photon.* **10**, 667–670 (2016).
- Vampa, G. et al. Plasmon-enhanced high-harmonic generation from silicon. *Nat. Phys.* **13**, 659–662 (2017).
- Ludwig, M. et al. Sub-femtosecond electron transport in a nanoscale gap. *Nat. Phys.* **16**, 341–345 (2020).
- Langer, F. et al. Lightwave valleytronics in a monolayer of tungsten diselenide. *Nature* **557**, 76–80 (2018).
- Borsch, M. et al. Super-resolution lightwave tomography of electronic bands in quantum materials. *Science* **370**, 1204–1207 (2020).
- Goulielmakis, E. & Brabec, T. High harmonic generation in condensed matter. *Nat. Photon.* **16**, 411–421 (2022).
- Dienstbier, P. et al. Tracing attosecond electron emission from a nanometric metal tip. *Nature* **616**, 702–706 (2023).
- Paschen, T. et al. Ultrafast strong-field electron emission and collective effects at a one-dimensional nanostructure. *ACS Photonics* **10**, 447–455 (2023).
- Booake, T. et al. Light-field control of real and virtual charge carriers. *Nature* **605**, 251–255 (2022).
- Krausz, F. & Ivanov, M. Attosecond physics. *Rev. Mod. Phys.* **81**, 163–234 (2009).
- Baltuška, A. et al. Attosecond control of electronic processes by intense light fields. *Nature* **421**, 611–615 (2003).
- Wittmann, T. et al. Single-shot carrier-envelope phase measurement of few-cycle laser pulses. *Nat. Phys.* **5**, 357–362 (2009).
- Goulielmakis, E. et al. Single-cycle nonlinear optics. *Science* **320**, 1614–1617 (2008).
- Cederbaum, L. & Zobeley, J. Ultrafast charge migration by electron correlation. *Chem. Phys. Lett.* **307**, 205–210 (1999).
- Remacle, F., Levine, R. D., Schlag, E. W. & Weinkauff, R. Electronic control of site selective reactivity: a model combining charge migration and dissociation. *J. Phys. Chem. A* **103**, 10149–10158 (1999).
- Lünnemann, S., Kuleff, A. I. & Cederbaum, L. S. Ultrafast charge migration in 2-phenylethyl-*N,N*-dimethylamine. *Chem. Phys. Lett.* **450**, 232–235 (2008).
- Breidbach, J. & Cederbaum, L. S. Migration of holes: formalism, mechanisms, and illustrative applications. *J. Chem. Phys.* **118**, 3983–3996 (2003).
- Remacle, F. & Levine, R. D. An electronic time scale in chemistry. *Proc. Natl Acad. Sci. USA* **103**, 6793–6798 (2006).
- Kuleff, A. I. & Cederbaum, L. S. Ultrafast correlation-driven electron dynamics. *J. Phys. B: At. Mol. Opt. Phys.* **47**, 124002 (2014).
- Calegari, F., Sansone, G., Stagira, S., Vozzi, C. & Nisoli, M. Advances in attosecond science. *J. Phys. B: At. Mol. Opt. Phys.* **49**, 062001 (2016).
- Basov, D., Averitt, R. & Hsieh, D. Towards properties on demand in quantum materials. *Nat. Mater.* **16**, 1077–1088 (2017).
- Giannetti, C. et al. Ultrafast optical spectroscopy of strongly correlated materials and high-temperature superconductors: a non-equilibrium approach. *Adv. Phys.* **65**, 58–238 (2016).
- de la Torre, A. et al. Colloquium: nonthermal pathways to ultrafast control in quantum materials. *Rev. Mod. Phys.* **93**, 041002 (2021).
- Kuroda, K. et al. Evidence for magnetic Weyl fermions in a correlated metal. *Nat. Mater.* **16**, 1090–1095 (2017).
- Yin, J.-X. et al. Giant and anisotropic many-body spin-orbit tunability in a strongly correlated Kagome magnet. *Nature* **562**, 91–95 (2018).
- Bradlyn, B. et al. Beyond Dirac and Weyl fermions: unconventional quasiparticles in conventional crystals. *Science* **353**, aaf5037 (2016).
- Topp, G. E., Tancogne-Dejean, N., Kemper, A. F., Rubio, A. & Sentef, M. A. All-optical nonequilibrium pathway to stabilising magnetic Weyl semimetals in pyrochlore iridates. *Nat. Commun.* **9**, 4452 (2018).
- Fausti, D. et al. Light-induced superconductivity in a stripe-ordered cuprate. *Science* **331**, 189–191 (2011).
- Mitrano, M. et al. Possible light-induced superconductivity in K_3C_{60} at high temperature. *Nature* **530**, 461–464 (2016).
- Buzzi, M. et al. Photomolecular high-temperature superconductivity. *Phys. Rev. X* **10**, 031028 (2020).
- Uzan-Narovlansky, A. J. et al. Observation of light-driven band structure via multiband high-harmonic spectroscopy. *Nat. Photon.* **16**, 428–432 (2022).
- Baykushcheva, D. R. et al. Ultrafast renormalization of the on-site Coulomb repulsion in a cuprate superconductor. *Phys. Rev. X* **12**, 011013 (2022).

52. Oka, T. & Aoki, H. Photovoltaic Hall effect in graphene. *Phys. Rev. B* **79**, 081406 (2009).
53. Oka, T. & Kitamura, S. Floquet engineering of quantum materials. *Annu. Rev. Condens. Matter Phys.* **10**, 387–408 (2019).
54. Mikami, T. et al. Brillouin-Wigner theory for high-frequency expansion in periodically driven systems: application to Floquet topological insulators. *Phys. Rev. B* **93**, 144307 (2016).
55. Mentink, J., Balzer, K. & Eckstein, M. Ultrafast and reversible control of the exchange interaction in Mott insulators. *Nat. Commun.* **6**, 6708 (2015).
56. Ito, S. et al. Build-up and dephasing of Floquet-Bloch bands on subcycle timescales. *Nature* **616**, 696–701 (2023).
57. Tsuji, N., Oka, T., Aoki, H. & Werner, P. Repulsion-to-attraction transition in correlated electron systems triggered by a monocycle pulse. *Phys. Rev. B* **85**, 155124 (2012).
58. Tsuji, N., Oka, T., Werner, P. & Aoki, H. Dynamical band flipping in fermionic lattice systems: an a.c.-field-driven change of the interaction from repulsive to attractive. *Phys. Rev. Lett.* **106**, 236401 (2011).
59. Schultze, M. et al. Delay in photoemission. *Science* **328**, 1658–1662 (2010).
60. Ossiander, M. et al. Absolute timing of the photoelectric effect. *Nature* **561**, 374–377 (2018).
61. Sommer, A. et al. Attosecond nonlinear polarization and light-matter energy transfer in solids. *Nature* **534**, 86–90 (2016).
62. Schmid, C. P. et al. Tunable non-integer high-harmonic generation in a topological insulator. *Nature* **593**, 385–390 (2021).
63. Putnam, W. P., Hobbs, R. G., Keathley, P. D., Berggren, K. K. & Kärtner, F. X. Optical-field-controlled photoemission from plasmonic nanoparticles. *Nat. Phys.* **13**, 335–339 (2017).
64. Higuchi, T., Heide, C., Ullmann, K., Weber, H. B. & Hommelhoff, P. Light-field-driven currents in graphene. *Nature* **550**, 224–228 (2017).
65. Lakhota, H. et al. Laser picoscopy of valence electrons in solids. *Nature* **583**, 55–59 (2020).
66. Joura, A. V., Freericks, J. & Lichtenstein, A. I. Long-lived nonequilibrium states in the Hubbard model with an electric field. *Phys. Rev. B* **91**, 245153 (2015).
67. Murakami, Y., Eckstein, M. & Werner, P. High-harmonic generation in Mott insulators. *Phys. Rev. Lett.* **121**, 057405 (2018).
68. Aron, C., Kotliar, G. & Weber, C. Dimensional crossover driven by an electric field. *Phys. Rev. Lett.* **108**, 086401 (2012).
69. Schmidt, P. & Monien, H. Nonequilibrium dynamical mean-field theory of a strongly correlated system. Preprint at <https://doi.org/10.48550/arXiv.cond-mat/0202046> (2022).
70. Tsuji, N., Oka, T. & Aoki, H. Correlated electron systems periodically driven out of equilibrium: Floquet+DMFT formalism. *Phys. Rev. B* **78**, 235124 (2008).
71. Aoki, H. et al. Nonequilibrium dynamical mean-field theory and its applications. *Rev. Mod. Phys.* **86**, 779 (2014).
72. Georges, A., Kotliar, G., Krauth, W. & Rozenberg, M. J. Dynamical mean-field theory of strongly correlated fermion systems and the limit of infinite dimensions. *Rev. Mod. Phys.* **68**, 13 (1996).
73. Eckstein, M., Kollar, M. & Werner, P. Interaction quench in the Hubbard model: relaxation of the spectral function and the optical conductivity. *Phys. Rev. B* **81**, 115131 (2010).
74. Schüler, M. et al. NESSi: the non-equilibrium systems simulation package. *Comput. Phys. Commun.* **257**, 107484 (2020).
75. Markiewicz, R. S., Sahrakorpi, S., Lindroos, M., Lin, H. & Bansil, A. One-band tight-binding model parametrization of the high- T_c cuprates including the effect of k_z dispersion. *Phys. Rev. B* **72**, 054519 (2005).
76. Delannoy, J.-Y. P., Gingras, M. J. P., Holdsworth, P. C. W. & Tremblay, A.-M. S. Low-energy theory of the $t-t'-t''-U$ Hubbard model at half-filling: interaction strengths in cuprate superconductors and an effective spin-only description of La_2CuO_4 . *Phys. Rev. B* **79**, 235130 (2009).
77. Wu, W., Ferrero, M., Georges, A. & Kozik, E. Controlling Feynman diagrammatic expansions: physical nature of the pseudogap in the two-dimensional Hubbard model. *Phys. Rev. B* **96**, 041105 (2017).
78. Sakakibara, H. et al. Model-mapped RPA for determining the effective Coulomb interaction. *J. Phys. Soc. Jpn* **86**, 044714 (2017).
79. Honerkamp, C. Efficient vertex parametrization for the constrained functional renormalization group for effective low-energy interactions in multiband systems. *Phys. Rev. B* **98**, 155132 (2018).
80. Schmid, M. T., Morée, J.-B., Yamaji, Y. & Imada, M. Superconductivity studied by solving ab initio low-energy effective Hamiltonians for carrier doped CaCuO_2 , $\text{Bi}_2\text{Sr}_2\text{CuO}_6$, $\text{Bi}_2\text{Sr}_2\text{CaCu}_2\text{O}_8$, and $\text{HgBa}_2\text{CuO}_4$. *Phys. Rev. X* **13**, 041036 (2023).
81. Kotliar, G. & Vollhardt, D. Strongly correlated materials: insights from dynamical mean-field theory. *Phys. Today* **57**, 53–59 (2004).
82. Reimann, K., Woerner, M. & Elsaesser, T. Two-dimensional terahertz spectroscopy of condensed-phase molecular systems. *J. Chem. Phys.* **154**, 120901 (2021).
83. Randi, F., Fausti, D. & Eckstein, M. Bypassing the energy-time uncertainty in time-resolved photoemission. *Phys. Rev. B* **95**, 115132 (2017).
84. Roudnev, V. & Esry, B. D. General theory of carrier-envelope phase effects. *Phys. Rev. Lett.* **99**, 220406 (2007).
85. Först, M. et al. Nonlinear phononics as an ultrafast route to lattice control. *Nat. Phys.* **7**, 854–856 (2011).
86. Kretschmar, M. et al. Compact realization of all-attosecond pump-probe spectroscopy. Preprint at <https://doi.org/10.48550/arXiv.2306.16212> (2023).
87. Dahlström, J. & Maquet, A. et al. Probing single-photon ionization on the attosecond time scale. *Phys. Rev. Lett.* **106**, 143002 (2011).
88. Travers, J. C., Grigorova, T. F., Brahms, C. & Belli, F. High-energy pulse self-compression and ultraviolet generation through soliton dynamics in hollow capillary fibres. *Nat. Photon.* **13**, 547–554 (2019).
89. Koll, L.-M., Maikowski, L., Drescher, L., Witting, T. & Vrakking, M. J. Experimental control of quantum-mechanical entanglement in an attosecond pump-probe experiment. *Phys. Rev. Lett.* **128**, 043201 (2022).
90. Azoury, D. et al. Interferometric attosecond lock-in measurement of extreme-ultraviolet circular dichroism. *Nat. Photon.* **13**, 198–204 (2019).
91. Kneller, O. et al. A look under the tunnelling barrier via attosecond-gated interferometry. *Nat. Photon.* **16**, 304–310 (2022).

Publisher's note Springer Nature remains neutral with regard to jurisdictional claims in published maps and institutional affiliations.

Open Access This article is licensed under a Creative Commons Attribution 4.0 International License, which permits use, sharing, adaptation, distribution and reproduction in any medium or format, as long as you give appropriate credit to the original author(s) and the source, provide a link to the Creative Commons license, and indicate if changes were made. The images or other third party material in this article are included in the article's Creative Commons license, unless indicated otherwise in a credit line to the material. If material is not included in the article's Creative Commons license and your intended use is not permitted by statutory regulation or exceeds the permitted use, you will need to obtain permission directly from the copyright holder. To view a copy of this license, visit <http://creativecommons.org/licenses/by/4.0/>.

© The Author(s) 2024

Methods

Simulations

The Hamiltonian is

$$H(t) = \sum_{ij\sigma} T_{ij}(t) c_{i\sigma}^\dagger c_{j\sigma} + U \sum_i \left(n_{i\uparrow} - \frac{1}{2} \right) \left(n_{i\downarrow} - \frac{1}{2} \right), \quad (4)$$

where i and j label the lattice sites, U is the on-site Coulomb interaction, $c_{i\sigma}^\dagger$ ($c_{i\sigma}$) are the fermionic creation (annihilation) operators for site i (j) and spin σ , and $n_{i\sigma} = c_{i\sigma}^\dagger c_{i\sigma}$ is the particle number operator. The hopping amplitudes $T_{ij}(t)$ between the sites i and j include the nearest-neighbour (T_1) and next-nearest-neighbour (T_2) terms. The external low-frequency laser field (frequency $\omega < U$, $W = 8T_1$) is included via the Peierls substitution:

$$T_{ij}(t) = T_{ij} \exp \left(-i \int_{\mathbf{R}_j}^{\mathbf{R}_i} \mathbf{dr} \cdot \mathbf{A}(t) \right), \quad (5)$$

where $\mathbf{A}(t)$ is the field-vector potential and $\mathbf{F}(t) = -\partial \mathbf{A}(t) / \partial t$. The one-particle dispersion is

$$\varepsilon(\mathbf{k}, t) = 2T_1 [\cos(k_x + \mathbf{A}_x(t)) + \cos(k_y + \mathbf{A}_y(t))] + 4T_2 [\cos(k_x + \mathbf{A}_x(t)) \cdot \cos(k_y + \mathbf{A}_y(t))]. \quad (6)$$

The total energy $E_{\text{tot}}(t) = E_{\text{kin}}(t) + E_{\text{pot}}(t)$ includes potential and kinetic terms, namely,

$$E_{\text{pot}}(t) = U \left\langle \left(n_{\uparrow} - \frac{1}{2} \right) \left(n_{\downarrow} - \frac{1}{2} \right) \right\rangle, \quad (7)$$

$$E_{\text{kin}}(t) = -i \sum_{\mathbf{k}} \varepsilon_{\mathbf{k}} \tilde{G}_{\mathbf{k}+\mathbf{A}(t)}^<(t, t), \quad (8)$$

respectively, where $\tilde{G}_{\mathbf{k}}^<(t, t)$ is the gauge-invariant⁷⁰ lesser Green's function. The momentum distribution function is

$$n(\mathbf{k}, t) = f(\mathbf{k}, t) = -i \tilde{G}_{\mathbf{k}}^<(t, t) = -i \tilde{G}_{\mathbf{k}+\mathbf{A}(t)}^<(t, t). \quad (9)$$

The population density is calculated as

$$G^<(\omega, t) = \frac{1}{\pi} \text{Im} \int ds e^{i\omega s} G^<(t, t-s). \quad (10)$$

Due to the limitation in time data, the selected Fourier transform produces some blur on the graph of the occupied states for the first 5 fs.

The time-resolved photoemission intensity is given by

$$I(\omega, t_p) = -i \int dt dt' S(t) S(t') e^{i\omega(t-t')} G^<(t + t_p, t' + t_p), \quad (11)$$

where $S(t - t_p)$ is the envelope of the probe pulse centred at t_p (ref. 92).

Direct access to non-adiabatic many-body dynamics

Here we develop the strategy for isolating the non-adiabatic response in the one-particle Green's function. In a long laser pulse, the dependence of the instantaneous electric field on the CEP amounts to the overall time shift $t = t' + t_{\text{CEP}}$. This trivial dependence is of no interest and should be removed when analysing Green's function $G_{ij}^<(t, t - \tau, t_{\text{CEP}})$. To see how this should be done, let us assume—for a moment—that its CEP dependence amounts only to the overall time shift in the argument $t = t' + t_{\text{CEP}}$:

$$\tilde{G}_{ij}^<(t, t - \tau, t_{\text{CEP}}) = \tilde{G}_{ij}^<(t', t' - \tau). \quad (12)$$

If this is the case, Green's function should obey the following equation:

$$\frac{\partial G_{ij}^<}{\partial t}(t, t - \tau, t_{\text{CEP}}) = \frac{\partial G_{ij}^<}{\partial t_{\text{CEP}}}(t, t - \tau, t_{\text{CEP}}). \quad (13)$$

Therefore, differentiating Green's function $G_{ij}^<(t, t - \tau, t_{\text{CEP}})$ with respect to t and t_{CEP} and subtracting the resulting terms, we obtain the differential contribution $\Delta G_{ij}^<(t, t - \tau, t_{\text{CEP}})$, which no longer contains trivial dependence:

$$\Delta G_{ij}^<(t, t - \tau, t_{\text{CEP}}) = \frac{\partial G_{ij}^<}{\partial t}(t, t - \tau, t_{\text{CEP}}) - \frac{\partial G_{ij}^<}{\partial t_{\text{CEP}}}(t, t - \tau, t_{\text{CEP}}). \quad (14)$$

We use $\Delta G_{ij}^<(t, t - \tau, t_{\text{CEP}})$ for building the 2D spectroscopy maps as a function of Ω_t and Ω_{CEP} .

Now, we can explicitly evaluate $\Delta G_{ij}^<(t, t - \tau, t_{\text{CEP}})$ (equation (14)) for an arbitrary Hamiltonian $H(t)$.

Since we consider coherent dynamics, we can rewrite equation (16) for Green's function as follows^{93,94}:

$$G_{ij}^<(t, t - \tau) = i \sum_m \langle \Psi_m(t_0) | c_i^\dagger(t - \tau) c_j(t) | \Psi_m(t_0) \rangle, \quad (15)$$

where $|\Psi_m(t_0)\rangle$ are the field-free eigenstates of the system and t_0 is the initial moment before the laser pulse. Inserting the resolution of identity $I = \sum_n |\Psi_n(t_0)\rangle \langle \Psi_n(t_0)|$ on the field-free eigenstates, we get

$$G_{ij}^<(t, t - \tau) = i \sum_{m,n} \langle \Psi_m(t_0) | c_i^\dagger(t - \tau) | \Psi_n(t_0) \rangle \langle \Psi_n(t_0) | c_j(t) | \Psi_m(t_0) \rangle, \quad (16)$$

and switching from the Heisenberg to Schrödinger picture by transforming the temporal dependence from the operators to the wavefunctions, we obtain

$$G_{ij}^<(t, t - \tau) = i \sum_{m,n} \langle \Psi_m(t - \tau) | c_i^\dagger | \Psi_n(t - \tau) \rangle \langle \Psi_n(t) | c_j | \Psi_m(t) \rangle, \quad (17)$$

where $|\Psi_m(t)\rangle$ are time-dependent basis states evolving from the field-free states under the influence of the full propagator: $|\Psi_m(t)\rangle = \mathcal{T} e^{-i \int_0^t H(t') dt'} |\Psi_m(t_0)\rangle$, where \mathcal{T} is a time-ordering operator. Since the evolution is unitary, the time-dependent basis states remain orthogonal to each other at any time t within the pulse.

Since our Hamiltonian explicitly depends on t and t_{CEP} , $H(f(t), t + t_{\text{CEP}})$, where $f(t)$ is a short pulse envelope, the derivatives of the Hamiltonian with respect to each time can be explicitly calculated:

$$\frac{\partial H}{\partial t} = \frac{\partial H}{\partial f} \frac{\partial f}{\partial t} + \frac{\partial H}{\partial t_{\text{CEP}}}. \quad (18)$$

This yields

$$\Delta H = \frac{\partial H}{\partial f} \frac{\partial f}{\partial t}, \quad (19)$$

where we have introduced an operator $\Delta \equiv \frac{\partial}{\partial t} - \frac{\partial}{\partial t_{\text{CEP}}}$. To evaluate $\Delta G_{ij}^<(t, t - \tau)$, we take into account the fact that one can rewrite the Schrödinger equation for $\Delta \Psi_m$ in the equivalent form explicitly connecting ΔH and $\Delta \Psi_m$ ($|\Psi_m(t_0)\rangle = 0$):

$$|\Delta \Psi_m(t)\rangle = -i \int_{t_0}^t dt' \mathcal{T} e^{-i \int_{t_0}^{t'} H(t'') dt''} \Delta H \mathcal{T} e^{-i \int_{t_0}^{t'} H(t'') dt''} |\Psi_m(t_0)\rangle. \quad (20)$$

Explicitly writing $\Delta G_{ij}^<$, we obtain

$$\Delta G_{ij}^< = i \sum_{m,n} \langle \Delta \Psi_m(t - \tau) | c_i^\dagger | \Psi_n(t - \tau) \rangle \langle \Psi_n(t) | c_j | \Psi_m(t) \rangle + \quad (21)$$

$$i \sum_{m,n} \langle \Psi_m(t-\tau) | c_i^\dagger | \Delta \Psi_p(t-\tau) \rangle \langle \Psi_n(t) | c_j | \Psi_m(t) \rangle + \quad (22)$$

$$i \sum_{m,n} \langle \Psi_m(t-\tau) | c_i^\dagger | \Psi_n(t-\tau) \rangle \langle \Delta \Psi_n(t) | c_j | \Psi_m(t) \rangle + \quad (23)$$

$$i \sum_{m,n} \langle \Psi_m(t-\tau) | c_i^\dagger | \Psi_n(t-\tau) \rangle \langle \Psi_n(t) | c_j | \Delta \Psi_m(t) \rangle. \quad (24)$$

Substituting equation (20) into the above equations and limiting ourselves to the terms of the leading order with respect to $\frac{\partial}{\partial t}$ and $\frac{\partial}{\partial \tau}$, we find that $\Delta G_{ij}^<$ is proportional to the amplitudes of non-adiabatic transitions $a_{mp}(t) = \langle \Psi_m(t) | \frac{\partial}{\partial t} | \Psi_p(t) \rangle$ and between the quasienergy states:

$$\begin{aligned} \Delta G_{ij}^< = & - \sum_{m,p} f(t) a_{mp}(t) \langle \Psi_p(t_0) | [c_j(t), H^H(t)] c_i^\dagger(t-\tau) | \Psi_m(t_0) \rangle + \\ & + \sum_{m,p} f(t-\tau) a_{mp}(t-\tau) \langle \Psi_p(t_0) | [c_i^\dagger(t-\tau), H^H(t-\tau)] c_j(t) | \Psi_m(t_0) \rangle, \end{aligned} \quad (25)$$

where $H^H(t-\tau)$ is the Hamiltonian operator in the Heisenberg picture. Substituting the explicit expressions for the commutators $[c_i^\dagger(t-\tau), H^H(t-\tau)]$ and $[c_j(t), H^H(t)]$ for the Hubbard model and focusing on the correlated part of the Hamiltonian $H_2 = U \sum_{i,\sigma} n_{i,\sigma} n_{i+\sigma}$:

$$[c_i^\dagger(t-\tau), H_2^H(t-\tau)] = -U c_{i,\sigma}^\dagger(t-\tau) n_{i,\bar{\sigma}}(t-\tau), \quad (26)$$

$$[c_j(t), H_2^H(t)] = U c_{i,\sigma}(t) n_{i,\bar{\sigma}}(t). \quad (27)$$

We obtain that $\Delta G_{ij}^<$ ($\Delta G_{ij}^<$) (Fig. 3) directly reflects the non-equilibrium two-body Green's functions $K_{ij\sigma}^{pm}(t, t-\tau)$ and $\tilde{K}_{ij\sigma}^{pm}(t, t-\tau)$:

$$\begin{aligned} \Delta G_{ij\sigma}^<(t, t-\tau) = & - \sum_{m,p} f(t-\tau) a_{mp}(t-\tau) K_{ij\sigma}^{pm}(t, t-\tau) \\ & - \sum_{m,p} f(t) a_{mp}(t) \tilde{K}_{ij\sigma}^{pm}(t, t-\tau) + \Delta G_{ij\sigma}^{(1)<}, \end{aligned} \quad (28)$$

where $f(t)$ is the envelope of the short pulse, $a_{mp}(t) = \langle \Psi_m(t) | \frac{\partial}{\partial t} | \Psi_p(t) \rangle$ is the amplitude of non-adiabatic transitions between the time-dependent states evolving from the field-free eigenstates $|\Psi_m(t_0)\rangle$ and $|\Psi_p(t_0)\rangle$, $\Delta G_{ij\sigma}^{(1)<}$ are the non-adiabatic terms of one-particle nature and

$$K_{ij\sigma}^{pm}(t, t-\tau) = U \langle \Psi_p(t_0) | c_{i\sigma}^\dagger(t-\tau) n_{i\bar{\sigma}}(t-\tau) c_{j\sigma}(t) | \Psi_m(t_0) \rangle, \quad (29)$$

$$\tilde{K}_{ij\sigma}^{pm}(t, t-\tau) = U \langle \Psi_p(t_0) | c_{j\sigma}(t) n_{i\bar{\sigma}}(t) c_{i\sigma}^\dagger(t-\tau) | \Psi_m(t_0) \rangle. \quad (30)$$

Here U is the on-site Coulomb interaction, $c_{i\sigma}^\dagger$ ($c_{i\sigma}$) are the fermionic creation (annihilation) operators for site i (j) and spin σ . Also, $n_{i\sigma} = c_{i\sigma}^\dagger c_{i\sigma}$ is the particle number operator. Note that in contrast with the standard equilibrium (diagonal in m) expressions of

$$K_{ij\sigma}^{mm}(t, t-\tau) = U \langle \Psi_m(t_0) | c_{i\sigma}^\dagger(t-\tau) n_{i\bar{\sigma}}(t-\tau) c_{j\sigma}(t) | \Psi_m(t_0) \rangle, \quad (31)$$

$$\tilde{K}_{ij\sigma}^{mm}(t, t-\tau) = U \langle \Psi_m(t_0) | c_{j\sigma}(t) n_{i\bar{\sigma}}(t) c_{i\sigma}^\dagger(t-\tau) | \Psi_m(t_0) \rangle, \quad (32)$$

which would appear in $\partial G_{ij\sigma}/\partial t$, off-diagonal $K_{ij\sigma}^{pm}(t, t-\tau)$ and $\tilde{K}_{ij\sigma}^{pm}(t, t-\tau)$ in equations (29) and (30), respectively, feature non-equilibrium two-particle correlations, which would not be recorded in long pulses ($\Delta G_{ij}^< = 0$), corresponding to the standard regime of cycle-averaged field-driven dynamics, which lays at the foundations of Floquet engineering.

Recovering full Green's function from photoelectron measurements

Although time- and angle-resolved photoemission experiments are directly related to Green's function, going back from time- and angle-resolved photoemission to Green's function is non-trivial. In particular, analysing the photoemission from a single pulse is restricted by energy-time uncertainty⁹². Multipulse spectroscopy does not suffer

from this limitation and allows for the full retrieval of Green's function, as discussed in other work⁸³ and in the discussion below.

The full information in Green's function can be retrieved by suitable measurements, for example, by exploiting the dependence of the photoemission signal on the phase delay between interfering parts of the photoemission pulse⁸³. With this in mind, we can say that $G^<(t, t-\tau)$ emulates the photoionization signal arising from the interference of two photoionization events at t and $t-\tau$.

To demonstrate how a time-resolved photoemission experiment may, in principle, resolve the full Green's function, we start from the general expression given in another work⁹² as

$$I(\omega, t_p) = \int dt dt' e^{i\omega(t-t')} (-i) G^<(t, t') s(t) s(t')^*, \quad (33)$$

where orbital and momentum indices are omitted for simplicity, ω is the frequency of a probe pulse and $s(t)$ is its envelope. Evidently, a single Gaussian probe pulse of width δt implies a measurement of $G^<(\omega, t)$ with an uncertainty-limited filter in time and frequency. However, with suitable pulses, equation (33) shows that, in principle, the full-time dependence can be retrieved from experiment. For example, to measure $G^<(t, t')$ in a given time window, we choose an orthonormal basis $\phi_n(t)$ for time-dependent functions in that interval, and expand $-iG^<(t, t') = \sum_{n,n'} \phi_n^*(t) g_{n,n'} \phi_{n'}(t')$. The matrix $g_{n,n'}$ is Hermitian and positive definite. A probe pulse $S(t) = \phi_n(t)$ then measures the diagonal components, namely, $I = g_{n,n}$. A probe pulse $S(t) = \phi_n(t) + e^{i\varphi} \phi_m(t)$ gives $I = g_{n,n} + g_{m,m} + e^{-i\varphi} g_{n,m} + e^{i\varphi} g_{m,n}$; therefore, the off-diagonal components $g_{n,m}$ can be obtained by scanning the phase difference φ .

Spectroscopic nature of the double-time lesser Green's function

The double-time lesser Green's function provides information about the spectrum of occupied states of the system and is indispensable for visualizing the electronic structure and dynamics. We review the emergence of laser-dressed states in its structure using the approach presented in the 'Direct access to non-adiabatic many-body dynamics' section, starting from equation (17). Consider the typical Floquet regime corresponding to a continuous-wave pulse. The quasienergy states can be written as

$$\Psi_m(t) = e^{-i\varepsilon_m t} f_m(t), \quad \Psi_n(t) = e^{-i\varepsilon_n t} f_n(t), \quad (34)$$

where ε_m (ε_n) is the quasienergy of a Floquet state m (n) and $f_m(t)$ ($f_n(t)$) is a periodic function of time. Introducing auxiliary functions $\Phi_{nm}(t)$ and $\Phi_{mn}^{(+)}(t-\tau)$, that is,

$$\Phi_{nm}(t) \equiv \langle \Psi_n(t) | c_j | \Psi_m(t) \rangle = e^{i(\varepsilon_n - \varepsilon_m)t} f_{nm}(t), \quad (35)$$

$$\Phi_{mn}^{(+)}(t-\tau) \equiv \langle \Psi_m(t-\tau) | c_i^\dagger | \Psi_n(t-\tau) \rangle = e^{-i\varepsilon_n(t-\tau) + i\varepsilon_m(t-\tau)} f_{mn}(t-\tau), \quad (36)$$

we can rewrite the expression for Green's function as

$$G_{ij}^<(t, t-\tau) = i \sum_{m,n} \Phi_{mn}^{(+)}(t-\tau) \Phi_{nm}(t) = \sum_{m,n} f_{mn}(t-\tau) f_{nm}(t) e^{-i(\varepsilon_m - \varepsilon_n)\tau} \quad (37)$$

Since the functions $f_{mn}(t)$ and $f_{nm}(t-\tau)$ are periodic, we can expand them in a Fourier series:

$$f_{nm}(t) = \sum_k a_k^{nm} e^{i\omega_k t}, \quad (38)$$

$$f_{mn}(t-\tau) = \sum_{k'} a_{k'}^{mn} e^{-i\omega_{k'}(t-\tau)}. \quad (39)$$

Thus,

$$G_{ij}^<(t, t-\tau) = i \sum_{m,n} \sum_{k',l} a_{k'}^{mn} a_{l}^{nm} e^{-il\omega} e^{-i(\varepsilon_m - \varepsilon_n + k'\omega)\tau} \quad (40)$$

and the Fourier transform with respect to τ yields $\Omega_\tau = \varepsilon_m - \varepsilon_n + k'\omega$, where $\varepsilon_m - \varepsilon_n$ represents the spectral energy on the vertical axis (Fig. 1a,c,e). If we fix $\Omega_\tau = -1.25$ eV (LHB), then $k' = 0$. Fourier transforming equation (40) with respect to t , we obtain $\Omega_t = l\omega$ and a_l^{nm} are the

amplitudes of the Floquet ladder starting from zero energy, that is, the Floquet ladder corresponding to LHB for $\Omega_\tau = -1.25$ eV. Thus, in the standard Floquet picture, fixing $\Omega_\tau = E$ (as done in Fig. 3) leads to the observation of a standard Floquet ladder from state E .

The situation dramatically changes in the presence of non-adiabatic transitions between the Floquet states. Suppose such a non-adiabatic transition couples the Floquet state m to another Floquet state m' . Then,

$$\Phi_{nm}(t) = \lambda_{mm}(t)e^{i(\varepsilon_n - \varepsilon_m)t}f_{nm}(t) + \lambda_{m'm}(t)e^{i(\varepsilon_n - \varepsilon_{m'})t}f_{nm'}(t) \quad (41)$$

and

$$\begin{aligned} \Phi_{mn}^{(+)}(t - \tau) &= \lambda_{mm}(t - \tau)e^{-i(\varepsilon_n - \varepsilon_m)(t - \tau)}f_{mn}(t - \tau) \\ &+ \lambda_{mm'}(t - \tau)e^{-i(\varepsilon_n - \varepsilon_{m'})(t - \tau)}f_{m'n}(t - \tau), \end{aligned} \quad (42)$$

where the coefficients $\lambda_{mm'}(t)$ represent the amplitudes of non-adiabatic transitions between the quasienergies ε_m and $\varepsilon_{m'}$. In this case, the product $\Phi_{mn}(t - \tau)\Phi_{nm}(t)$, contributing to $G_{ij}^<(t, t - \tau)$ in equation (37), acquires three additional terms (equations (44)–(46)):

$$\Phi_{mn}(t - \tau)\Phi_{nm}(t) = \lambda_{mm}(t)\lambda_{mm}(t - \tau)f_{nm}(t)f_{mn}(t - \tau)e^{i(\varepsilon_n - \varepsilon_m)\tau} + \quad (43)$$

$$\lambda_{m'm}(t)\lambda_{mm}(t - \tau)f_{nm'}(t)f_{mn}(t - \tau)e^{i(\varepsilon_m - \varepsilon_{m'})t}e^{i(\varepsilon_n - \varepsilon_m)\tau} + \quad (44)$$

$$\lambda_{mm}(t)\lambda_{mm'}(t - \tau)f_{nm}(t)f_{m'n}(t - \tau)e^{i(\varepsilon_{m'} - \varepsilon_m)t}e^{i(\varepsilon_n - \varepsilon_{m'})\tau} + \quad (45)$$

$$\lambda_{m'm}(t)\lambda_{mm'}(t - \tau)f_{nm'}(t)f_{m'n}(t - \tau)e^{i(\varepsilon_n - \varepsilon_{m'})\tau}. \quad (46)$$

Non-adiabatic transitions from state with quasienergy ε_m to state with quasienergy $\varepsilon_{m'}$ lead to new features in the spectrum along both Ω_τ and Ω_t dimensions. Indeed, although the term in equation (43) is similar to that in equation (37), the term in equation (46) adds new frequency to the spectrum along the Ω_τ dimension. In addition, terms represented by equations (44) and (45) oscillate (in time t) at ‘new’ frequencies $\pm(\varepsilon_{m'} - \varepsilon_m)$, which will appear along the Ω_t direction. Thus, we see that non-adiabatic transitions lead to significant restructuring of the spectrum encoded in $G_{ij}^<(t, t - \tau)$ and are revealed after Fourier transforms with respect to τ and t .

To reveal the timescale of non-adiabatic transitions, we need to employ the additional dimension, sensitive to sub-laser-cycle features of electron dynamics. The CEP is a natural choice. Scanning CEP, we obtain $G_{ij}^<(t, t - \tau, t_{\text{CEP}})$. Fourier transform with respect to t_{CEP} (ref. 84) allows us to tag each non-adiabatic transition and quantify the role of sub-laser-cycle dynamics in restructuring the spectrum of the system as well as in the formation of the final insulating state.

Data availability

The data for Figs. 1–4 are available via GitHub at <https://github.com/vvalmispild/Sub-cycle-multidimensional-spectroscopy/tree/main>. Permission to access the data is available from the corresponding author upon reasonable request.

Code availability

The data presented in the manuscript were obtained by the time-dependent dynamical mean-field theory method within the Non-Equilibrium Systems Simulation (NESSi) package (its source code is subject to the terms of the Mozilla Public License v. 2.0; <https://github.com/nessi-cntr/nessi>).

References

92. Freericks, J., Krishnamurthy, H. & Pruschke, T. Theoretical description of time-resolved photoemission spectroscopy: application to pump-probe experiments. *Phys. Rev. Lett.* **102**, 136401 (2009).
93. Stefanucci, G. & van Leeuwen, R. *Nonequilibrium Many-Body Theory of Quantum Systems: A Modern Introduction* (Cambridge Univ. Press, 2013).
94. Kamenev, A. *Field Theory of Non-Equilibrium Systems* (Cambridge Univ. Press, 2011).

Acknowledgements

We thank M. Altarelli for motivating discussions, U. Bovensiepen and M. Ligges for discussions on the pump-probe photoemission of cuprates, R. E. F. Silva for providing his code for the benchmark and Y. Mohammed for checking the analytical calculations presented in equations (1)–(3) in the main text. This research was supported in part through the European XFEL and DESY computational resources in the Maxwell infrastructure operated at Deutsches Elektronen-Synchrotron (DESY), Hamburg, Germany. This work was supported by the Cluster of Excellence ‘Advanced Imaging of Matter’ of the Deutsche Forschungsgemeinschaft (DFG)—EXC 2056—project ID390715994. H.A. acknowledges support from the ImPACT Program of the Council for Science, Technology and Innovation, Cabinet Office, Government of Japan (grant no. 2015-PM12-05-01) from JST; JSPS KAKENHI grant no. 17H06138; and CREST ‘Topology’ project from JST. M.Y.I. and O.S. acknowledge support from the H2020 European Research Council Optologic grant (899794). The work of A.I.L. and M.I.K. is supported by the European Research Council via Synergy Grant 854843—FASTCORR. M.E. acknowledges funding from the ERC via starting grant no. 716648. The work of O.S. was funded by the European Union (ERC, ULISSES, 101054696). Views and opinions expressed are, however, those of the author(s) only and do not necessarily reflect those of the European Union or the European Research Council. Neither the European Union nor the granting authority can be held responsible for them.

Author contributions

The idea of the method was developed by O.S. The computations were performed by V.N.V. and E.G. All authors discussed the results and contributed to the preparation of the manuscript.

Funding

Open access funding provided by Max-Born-Institut für Nichtlineare Optik und Kurzzeitspektroskopie (MBI) im Forschungsverbund Berlin e.V.

Competing interests

The authors declare no competing interests.

Additional information

Supplementary information The online version contains supplementary material available at <https://doi.org/10.1038/s41566-023-01371-1>.

Correspondence and requests for materials should be addressed to O. Smirnova.

Peer review information *Nature Photonics* thanks Steven Cundiff, Claudio Giannetti and the other, anonymous, reviewer(s) for their contribution to the peer review of this work.

Reprints and permissions information is available at www.nature.com/reprints.